

Key Points:

- Down-front wind buoyancy forcing is stronger than heat loss buoyancy forcing in the western Irminger Sea
- We observe a subsurface ocean response to down-front winds consistent with slantwise convection
- Slantwise convection may mix waters to several times the conventionally defined mixed layer depth in this region

Correspondence to:

I. A.-A. Le Bras,
ilebras@whoi.edu

Citation:

Le Bras, I. A.-A., Callies, J., Straneo, F., Biló, T. C., Holte, J., & Johnson, H. L. (2022). Slantwise convection in the Irminger Sea. *Journal of Geophysical Research: Oceans*, 127, e2022JC019071. <https://doi.org/10.1029/2022JC019071>

Received 20 JUL 2022

Accepted 25 SEP 2022

Slantwise Convection in the Irminger Sea

I. A.-A. Le Bras¹ , J. Callies² , F. Straneo³ , T. C. Biló³ , J. Holte³ , and H. L. Johnson⁴ 

¹Woods Hole Oceanographic Institution, Woods Hole, MA, USA, ²California Institute of Technology, Pasadena, CA, USA,

³Scripps Institution of Oceanography, University of California San Diego, La Jolla, CA, USA, ⁴Department of Earth Sciences, University of Oxford, Oxford, Oxfordshire, UK

Abstract The subpolar North Atlantic is a site of significant carbon dioxide, oxygen, and heat exchange with the atmosphere. This exchange, which regulates transient climate change and prevents large-scale hypoxia throughout the North Atlantic, is thought to be mediated by vertical mixing in the ocean's surface mixed layer. Here we present observational evidence that waters deeper than the conventionally defined mixed layer are affected directly by atmospheric forcing in this region. When northerly winds blow along the Irminger Sea's western boundary current, the Ekman response pushes denser water over lighter water, potentially triggering slantwise convection. We estimate that this down-front wind forcing is four times stronger than air–sea heat flux buoyancy forcing and can mix waters to several times the conventionally defined mixed layer depth. Slantwise convection is not included in most large-scale ocean models, which likely limits their ability to accurately represent subpolar water mass transformations and deep ocean ventilation.

Plain Language Summary The deep ocean is an important part of the climate system, as it stores carbon dioxide and heat away from the atmosphere for hundreds to thousands of years. The transfer of properties between the atmosphere and deep ocean is broadly thought to occur in mixed layers formed by cooling at high-latitudes. Here we suggest that winds blowing in the same direction as ocean currents can trigger slantwise convection, which causes properties to be mixed to several times the conventionally defined mixed layer depth. We hypothesize that slantwise convection is active in the Irminger Sea as well as in western boundary currents across the subpolar North Atlantic region. Representing slantwise convection in ocean and climate models may be an important component of reproducing pathways into the deep ocean.

1. Introduction

In the high-latitude North Atlantic, warm, salty subtropical waters are transformed into the cold, fresh, oxygen- and carbon-rich waters that fill the deep ocean. The densest waters in the southward flowing lower limb of the Atlantic Meridional Overturning Circulation (AMOC) are Overflow Waters, which form in the Nordic Seas (Dickson & Brown, 1994; Huang et al., 2020), followed by Labrador Sea Water, which forms in deep mixed layers in the central Labrador and Irminger Seas (de Jong et al., 2018; Yashayaev & Loder, 2016b). These waters are observed throughout the deep North Atlantic (Swift, 1984; Talley & McCartney, 1982) and are often thought of as comprising the lower limb of the AMOC.

At the same time, there is growing appreciation that lighter waters formed near ocean boundaries are also a significant component of the AMOC's lower limb (Petit et al., 2020). These lighter waters include, in order of increasing density, eastern Subpolar Mode Waters (Brambilla & Talley, 2008; Brambilla et al., 2008), upper Irminger Sea Intermediate Water (Le Bras et al., 2020), and upper Labrador Sea Water (Pickart et al., 1996). Due to a dearth of year-round observations at the boundaries of the subpolar North Atlantic, however, the pathways and dynamics of this light portion of the AMOC's lower limb remain unclear.

One suggested mechanism of upper Labrador Sea Water formation is slantwise convection. Using an idealized model inspired by a handful of winter vertical density profiles, Straneo and coauthors hypothesized that winds blowing along the Labrador Sea's western boundary current cause an onshore Ekman transport that pushes denser water over lighter water and triggers slantwise convection (Straneo, Kawase, & Pickart, 2002; Straneo, Kawase, & Riser, 2002).

Slantwise convection is the response to a mixed convective–shear instability called symmetric instability and results in mixing approximately along isopycnals (Haine & Marshall, 1998; Thomas, 2005). Evidence of slantwise convection has been observed at strong currents and persistent fronts such as the Gulf Stream, Kuroshio,

and Antarctic Circumpolar Current (Joyce et al., 2009; Peng et al., 2020; Thomas et al., 2013, 2016; Viglione et al., 2018) as well as at transient fronts (Bosse et al., 2021; Buckingham et al., 2019; Thompson et al., 2016; Yu et al., 2019). Slantwise convection is thought to play a significant role in subtropical mode water formation (Joyce et al., 2013), in the reduction of the wind-work available to the large-scale ocean circulation (Thomas & Taylor, 2010), and in critically modifying turbulence in the ocean's surface boundary layer (D'Asaro et al., 2011). However, its role in the watermass transformations associated with the AMOC has not yet been demonstrated.

The subsurface ocean response to slantwise convection is usefully framed in terms of potential vorticity (PV). PV is set by atmospheric forcing at the sea surface and is conserved in the ocean interior in the absence of mixing or boundary interactions. So, a water parcel's PV contains its history of modification. Slantwise convection is triggered when negative PV arises through a combination of weak vertical buoyancy gradients and strong horizontal buoyancy gradients (or, equivalently, high geostrophic shear) (Giordani et al., 2017; Haine & Marshall, 1998; Hoskins, 1974; Straneo, Kawase, & Riser, 2002). Slantwise convection homogenizes PV along slanted paths, but does not homogenize density vertically (Thomas, 2005). Hence, slantwise convection leaves behind a stably stratified surface layer of homogeneous low PV, just as upright convection creates a layer of weak vertical stratification (Taylor & Ferrari, 2010).

Here we present evidence of slantwise convection in the western Irminger Sea from Overturning in the Subpolar North Atlantic Program (OSNAP) moored observations. The moorings are located near Cape Farewell, Greenland's southern tip, where flow distortions by Greenland's high topography cause extreme winds (Harden & Renfrew, 2012; Moore et al., 2008). In the winter and spring the winds are predominantly northerly and aligned with the Irminger Sea's southward-flowing western boundary current, which carries cold, fresh Arctic waters on the shelfbreak as well as warm, salty Atlantic Waters just offshore (Figure 1) (Daniault et al., 2011; Le Bras et al., 2018). These down-front winds push the denser, saltier water over lighter fresher water and appear to trigger slantwise convection (Figure 2). We find that boundary current waters are affected by this Ekman buoyancy forcing well below the surface mixed layer, suggesting a new mechanism for the transformation and ventilation of the light portion of the AMOC's lower limb. Though slantwise convection is likely significant throughout much of the western subpolar gyre, it is not accounted for in numerical models of this region.

2. Data and Methods

2.1. Mooring Data and Atmospheric Reanalysis

Our focus is on OSNAP mooring data in the western Irminger Sea at about 60°N from August 2014 to August 2018. The mooring data are linearly interpolated to a 2 dbar vertical grid and calibrated using Conductivity, Temperature, Depth (CTD) profiles measured during research cruises (Le Bras et al., 2018). A low-pass Butterworth filter with a 40 hr cutoff was applied to all data to remove the tidal signature. The shallowest instruments on each mooring range from 30 to 100 m. Upward-facing acoustic Doppler current profilers (ADCPs) measure the near-surface velocities (Figure 1b). Salinity and temperature are extrapolated by extending the shallowest measured gradient to the surface. Our analysis is focused on the winter and spring, when this is a sensible approximation. We use potential temperature and unitless practical salinity for consistency with past studies. Unless otherwise specified, we consider all properties and forcing at six-hourly resolution. Our analysis is restricted to 2014 to 2018 because an instrument loss on the CF5 mooring, which is the focus of our analysis, complicates the inclusion of the 2018 to 2020 record. The positions of all moorings referred to in this analysis are shown in Figures 1b and 1c, with the exception of mooring M1, which is situated at the 95 km mark.

Our calculations of the buoyancy flux associated with down-front winds, heat flux, and evaporation and precipitation are based on the ERA5 atmospheric reanalysis product. We also analyze ERA5 hourly sea level pressure fields. ERA5 is the fifth generation reanalysis product provided by the European Centre for Medium-Range Weather Forecast (ECMWF) (Dee et al., 2011), which runs from 1959 to the present. Data are provided gridded onto 0.25° x 0.25° from their original approximately 30 km resolution. We bin the hourly data to match the six-hourly mooring data.

2.2. PV, Zonal Absolute Momentum, and Mixed Layer Definitions

We use an across-section reference frame centered around mooring CF5: positive velocities are 11.7° clockwise from north. The across-section reference frame was chosen for the PV calculation as the only horizontal gradients

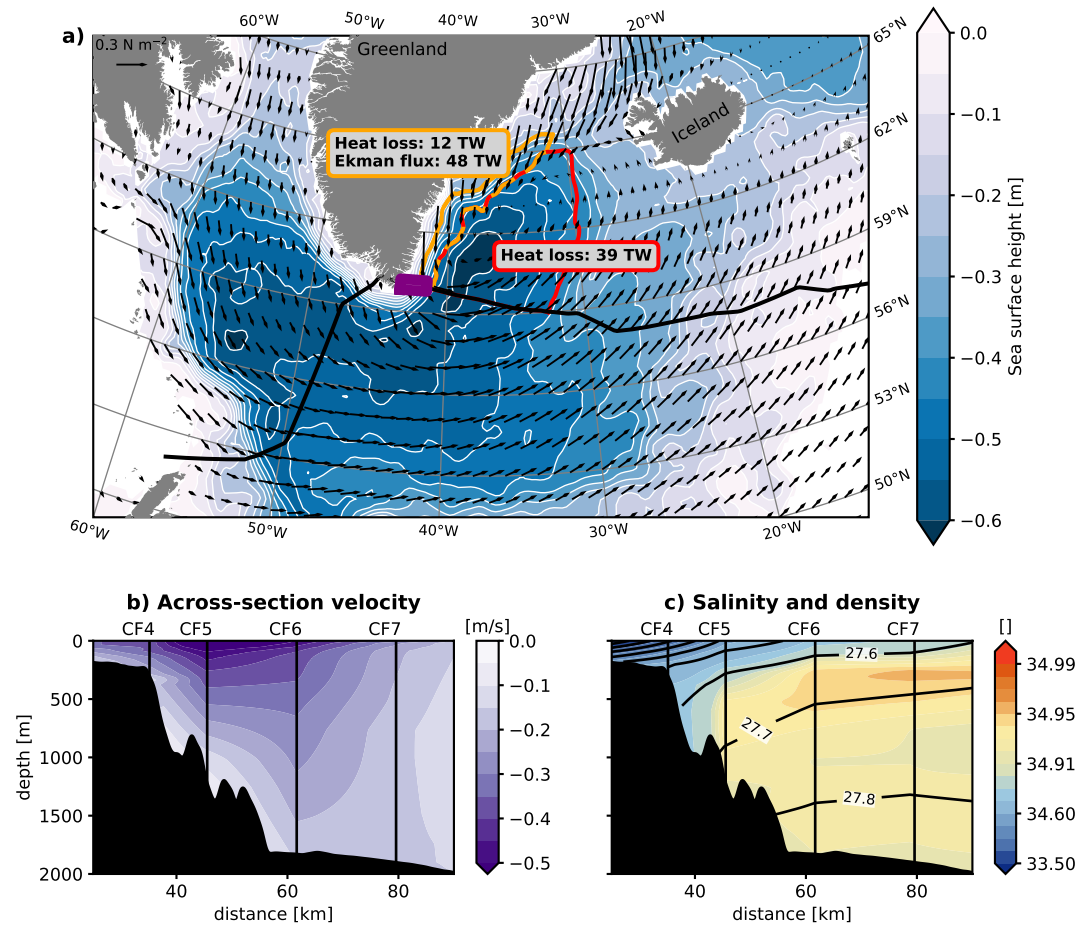


Figure 1. Regional context in winter and spring. All quantities in panels (a–c) are averaged over November–April, 2014–2018. (a) Wind stress (arrows) and sea surface height (contours) in the subpolar North Atlantic. The black line is the Overturning in the Subpolar North Atlantic Program section and the purple box highlights the location of the Cape Farewell moorings shown in panels (b) and (c). The red and orange lines indicate the Irminger interior and boundary regions bounded by the 2000 and 500 m isobaths; they are labeled with their time-mean spatially integrated air–sea heat flux loss and the deduced equivalent Ekman heat flux loss in the boundary region. (b) Across-mooring-line velocity measured by the moorings. (c) Observed salinity, shown with σ_θ isopycnals separated by 0.1 kg m^{-3} . The labeled vertical black lines in (b) and (c) indicate mooring positions.

we resolve with the moorings are in the along-section direction. Note that this is different from the angle used in Le Bras et al. (2018) and Le Bras et al. (2020) (23.3°), which was chosen to maximize boundary current transport.

PV is approximated as $(f + \zeta)N^2 - f v_z^2$, where f is the Coriolis parameter at 60°N , ζ is the relative vorticity of the across-section velocity, $N^2 = b_z$ is the buoyancy frequency, $b = -g\rho_\theta/\rho_0$ is buoyancy, $g = 9.8 \text{ m s}^{-2}$ is the earth's gravitational acceleration, ρ_θ is potential density, $\rho_0 = 1,027 \text{ kg m}^{-3}$ is a reference density, v is across-section velocity, and z subscripts denote vertical derivatives. This form of PV is a good first-order approximation and the most complete form of PV that can be calculated from our mooring observations. The velocity is smoothed into 100 m vertical bins before gradients are calculated from it. We have assumed thermal wind balance, $f v_z = b_x$, where b_x is the along-section buoyancy gradient. We substitute the horizontal buoyancy gradient with the vertical shear as horizontal buoyancy gradient measurements in the boundary current are limited by the continental slope and we find that the observations are generally consistent with thermal wind balance.

Zonal absolute momentum is calculated as $m = (f^* - b_x/f)z - fx$, following Straneo, Kawase, and Riser (2002), where $f^* = 2 \Omega \cos(\text{latitude})$, $\Omega = 7.2921 \times 10^{-5} \text{ rad s}^{-1}$ is the rotation rate of the earth, x is distance in the along-section direction and z is depth. Note that our zonal absolute momentum is in the along-section direction, which is nearly but not truly zonal.

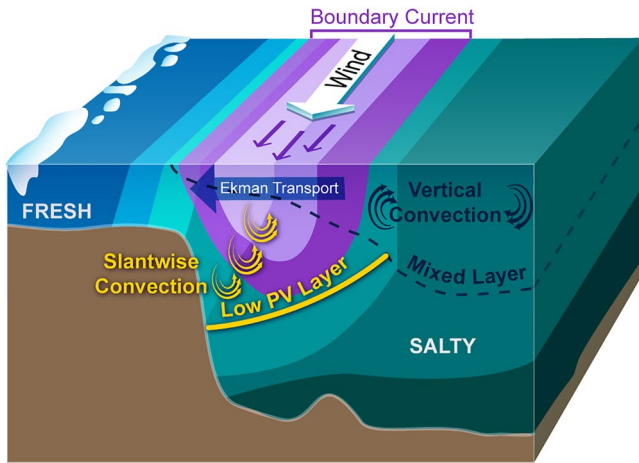


Figure 2. Schematic illustration of hypothesized slantwise convection in the Irminger Sea. The core of the boundary current is shown in purple, and the across-shore density gradient is represented by the transition from blue to green. Winds blowing in the same direction as the boundary current push salty, denser water over fresh, lighter water through the Ekman response. This triggers slantwise convection, which mixes water along slanted paths and creates a low-potential vorticity layer that is several times deeper than the mixed layer in the boundary current. The unstratified mixed layer, formed via cooling and upright convection, is deeper offshore.

The mixed layer is defined using a threshold of $\rho = 0.01 \text{ kg m}^{-3}$ relative to the potential density at 100 m, as this depth is fairly well-sampled. Mixed layer depths are averaged into 3-day bins for clarity in the figures, and to highlight mixed layer persistence.

2.3. Buoyancy Forcing Calculations

The Ekman buoyancy forcing is given by $B_{\text{wind}} = -\tau^y b_x / \rho_0 f$, where τ^y is the wind stress in the across-section direction. Negative Ekman buoyancy forcing removes buoyancy from the ocean and is analogous to heat loss. Slantwise convection events are defined as times when the magnitude of the negative Ekman buoyancy forcing was greater than $2 \times 10^{-6} \text{ m}^2 \text{ s}^{-3}$, which is equivalent to almost $-8,000 \text{ W m}^{-2}$. This threshold is about three times the standard deviation of the Ekman buoyancy forcing, and was found to be the most inclusive threshold for which there was a consistent subsurface response. We identified all dates when this threshold was surpassed and centered each event around the maximum Ekman buoyancy forcing. Events were considered separate if the Ekman buoyancy forcing stayed below the threshold for more than 2 days.

The air–sea heat flux was converted into buoyancy forcing units using $B_0 = g\alpha Q_{\text{net}} / \rho_0 c_p$, where $\alpha = 1 \times 10^{-4} \text{ } ^\circ\text{C}^{-1}$ is the thermal expansion coefficient of seawater with absolute salinity of 34.9 g kg^{-1} , conservative temperature of 4°C , and zero pressure, Q_{net} is the air–sea heat loss, and $c_p = 3850 \text{ J kg}^{-1} \text{ } ^\circ\text{C}^{-1}$ is the specific heat capacity of seawater. Evaporation minus precipitation was

converted into equivalent buoyancy forcing units using $B_{e-p} = -g\beta S_{\text{sc}} (E - P)$, where $\beta = 7.7 \times 10^{-4}$ is the haline contraction coefficient calculated using the same parameters as α , S_{sc} is the salinity extrapolated to the surface at the mooring locations, and $E - P$ is the evaporation minus precipitation.

Our low-PV layer depth analysis is based on an equation derived by Taylor and Ferrari (2010):

$$H(t) = \sqrt{-\frac{2(1 + \epsilon + \gamma)(B_0 + B_{\text{wind}})}{N^2 - M^4/f^2}} t, \quad (1)$$

where $H(t)$ is the depth of the low-PV layer; ϵ and γ are entrainment coefficients; B_0 and B_{wind} are the air–sea and Ekman buoyancy forcing, respectively; N is the initial vertical buoyancy frequency; and M^2 is the horizontal buoyancy gradient. The inclusion of the horizontal gradient in the denominator accounts for slantwise effects, which modify both air–sea and Ekman buoyancy forcing (Straneo, Kawase, & Pickart, 2002).

The low-PV layer depth is sensitive to both the temporal resolution of the atmospheric forcing and the time scale over which the equation is integrated. To remove this time dependence, we estimate the ratio of this low-PV layer depth to the conventionally defined mixed layer depth, assuming that the equations for both depths are integrated over the same time period:

$$\frac{\text{Low PV layer depth}}{\text{Mixed layer depth}} = \frac{\sqrt{-(B_0 + B_{\text{wind}}) / (N^2 - M^4/f^2)}}{\sqrt{-B_0/N^2}} \quad (2)$$

where we have neglected all entrainment coefficients. Considering the positive entrainment coefficients would result in a deeper low-PV layer. So, neglecting the entrainment coefficients yields a conservative estimate. Note that these equations assume that buoyancy fluxes are negative (acting to deepen the low PV or mixed layer) and neglect re-stratification. Accordingly, we only calculate this ratio for each time at which both the air–sea and Ekman buoyancy forcing are negative, which is about one third of the record. We estimate N as the CF5 vertical buoyancy frequency at 200 m and M^2 as the horizontal buoyancy gradient at the surface.

3. Results

In the following sections we analyze down-front wind forcing events at the OSNAP Cape Farewell moorings. We first quantify the strength of the down-front wind forcing and find that it is several times stronger than the air–sea heat loss over the boundary current (Section 3.1). We then set an expectation for the subsurface response to this forcing using a theoretical parameterization and suggest that the forcing is strong enough to produce a low PV layer that is often several times deeper than the conventionally defined mixed layer (Section 3.2). Given this expectation, we analyze the subsurface mooring data during down-front wind forcing events and find that the evolution of the water mass structure (including the PV) is consistent with slantwise convection, though our data set does not resolve areas of negative PV (Section 3.3). Finally, we explore how down-front wind forcing may directly impact water mass transformations in this region (Section 3.4).

3.1. Ekman Buoyancy Forcing

The magnitude of the Ekman buoyancy forcing varies significantly across the boundary current (Figure 3c). This is due to the variation in along-section (across-front) buoyancy gradient, which is strongest at CF4 and decreases offshore (Figure 3a). The across-section (along-front) wind stress is relatively uniform across the moored array (Figure 3b). Both the buoyancy gradient and wind stress are episodic, with more frequent events of larger magnitude in the winter. The Ekman buoyancy forcing variability primarily matches the wind stress variability, but its strength is modulated by the buoyancy gradient.

The buoyancy forcing associated with air–sea heat fluxes and evaporation minus precipitation is relatively constant across the moored array (Figures 3d and 3e). Precipitation, which is restratifying and hence a positive buoyancy forcing, dominates in this region; evaporation is negligible compared to heat loss. Because our focus is on negative buoyancy forcing and a direct comparison with heat flux is informative and intuitive, we do not include precipitation and evaporation in the rest of our analysis.

Negative Ekman buoyancy forcing events can be over 10 times stronger than negative air–sea heat flux events (Figures 3c and 3d). In order to compare their net effect over the record, we time-integrate the buoyancy forcing and compare the cumulative negative Ekman buoyancy forcing with the cumulative heat loss buoyancy forcing (Figure 4). Note that in order to directly compare with heat loss and for consistency with the low-PV layer parameterization, we only include periods of negative buoyancy forcing in this calculation.

The time-integrated cumulative negative Ekman buoyancy forcing is largest at the onshore edge of the boundary current (CF4), where the buoyancy gradients are largest, and decreases offshore (Figure 4). At CF4, the cumulative negative Ekman buoyancy forcing is 8.5 times stronger than the cumulative air–sea heat flux forcing; at CF5 this ratio is 5. On the offshore edge of the boundary current, at CF6 and CF7, the cumulative negative Ekman buoyancy forcing is comparable to the cumulative air–sea heat flux forcing. Overall we find that the cumulative negative Ekman buoyancy forcing is about four times larger than the cumulative negative air–sea buoyancy forcing over the boundary current (orange and red lines in Figure 4).

3.2. Low-PV Layer Parameterization

We expect that the significant Ekman buoyancy forcing would trigger slantwise convection and result in a low-PV layer that is analogous to the mixed layer, but is not necessarily unstratified in terms of density (Taylor & Ferrari, 2010; Thomas, 2005). This low-PV layer can be thought of as the part of the water column affected by surface forcing. We estimate how the negative Ekman buoyancy forcing modifies the water column, relative to the impact of direct air–sea buoyancy forcing, by applying Equation 2 for the ratio between the low-PV layer depth and the classically defined mixed layer depth.

To investigate the impact of all terms on the ratio between the low-PV layer depth and the mixed layer depth, we calculate this ratio using only the air–sea buoyancy forcing, only the Ekman buoyancy forcing, and using both (Figure 5). Our analysis is focused on mooring CF5 because it experiences the strongest Ekman buoyancy forcing offshore of the shelfbreak and because lower limb AMOC waters have been observed at this site (Le Bras et al., 2020).

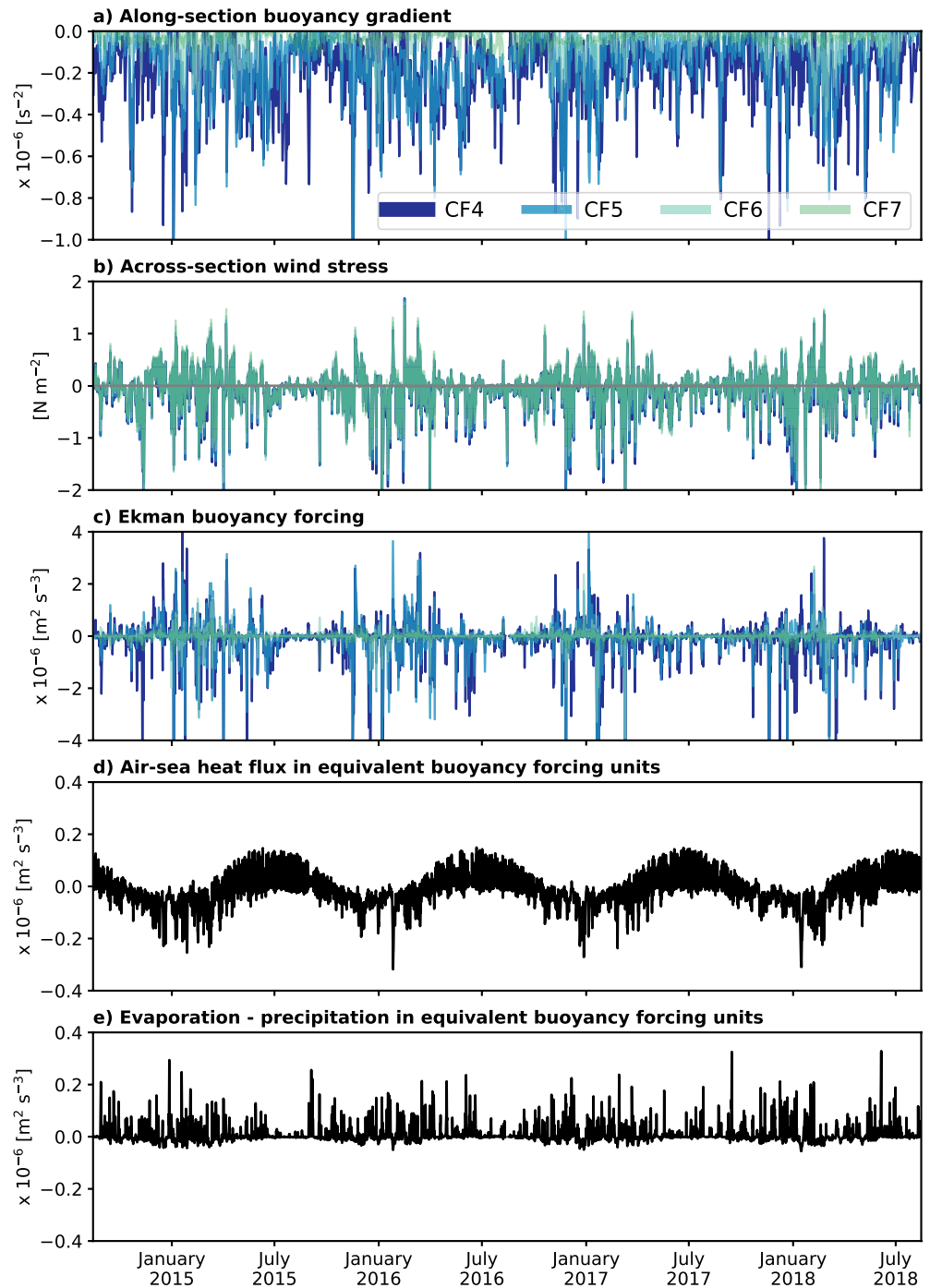


Figure 3. Buoyancy forcing and its components at the boundary current moorings (CF4–7) as labeled. The Ekman buoyancy forcing (panel c), is proportional to the product of the buoyancy gradient and wind stress (panels (a) and (b), respectively). Panels (d) and (e) show the mean across all four moorings. Note that the y-axes in panels d and e have one tenth of the range of panel (c).

When only the air–sea buoyancy forcing is included, the ratio is always greater than one, because the horizontal density gradient is always positive in the boundary current (Figure 5a). In other words, because of slantwise effects, the low-PV layer forced by air–sea buoyancy forcing is always deeper than the mixed layer (Straneo, Kawase, & Pickart, 2002). Our estimate of the ratio of the low-PV layer depth to the mixed layer depth forced by air–sea buoyancy flux alone falls between one and two on 95% of days, and has a mean value of 1.3 (Figure 5a).

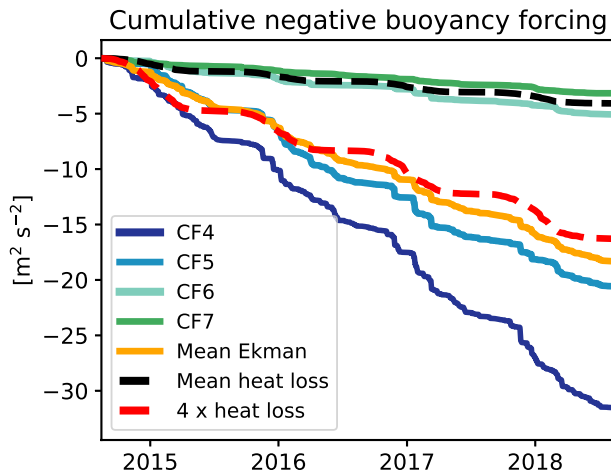


Figure 4. Cumulative negative Ekman buoyancy forcing (solid lines) estimated at the boundary current moorings, and the boundary current average (orange), shown with the cumulative negative buoyancy forcing associated with air–sea heat fluxes averaged over the boundary current (black dashed) as well as four times the air–sea heat fluxes for reference (red dashed).

When only the Ekman buoyancy forcing is included in Equation 1, the ratio of the low-PV layer depth to the conventional mixed layer depth can be less than one when the air–sea buoyancy forcing is greater than the Ekman buoyancy forcing scaled by the slantwise effect. However, we find that on 42% of the days we consider, the low-PV layer forced by Ekman buoyancy forcing is more than two times as deep as the mixed layer. In fact the mean value of this ratio considering Ekman buoyancy forcing alone is 3.6, and there are a significant number of days on which this ratio is larger than 5 (Figure 5b).

Considering both Ekman and air–sea buoyancy forcing (Equation 2), we find that the low-PV layer is more than two times deeper than the mixed layer on 57% of the days we consider, and the mean ratio is 4 (Figure 5c). The distribution is governed by the Ekman buoyancy forcing, particularly for larger ratios. In sum, our analysis suggests that there is a low-PV layer in the boundary current that is several times deeper than the conventionally defined mixed layer, and that its depth is controlled primarily by Ekman buoyancy forcing.

3.3. Subsurface Ocean Response

Our analysis of the expected low-PV layer depth suggests that strong down-front wind events will lead to decreased PV below the conventionally defined mixed layer depth. We find that this is the case within the boundary current (CF5), where dramatic drops in PV are observed in conjunction with strong Ekman buoyancy forcing events (Figure 6). These PV responses are observed well below the conventionally defined mixed layer depth at CF5, which is generally shallower than 300 m, and always shallower than 600 m (Figure 7a). Though some events have a clear response throughout the water column (e.g., late January 2017), the PV time series are noisy. In order to carefully examine the subsurface response to down-front events, we form a composite event.

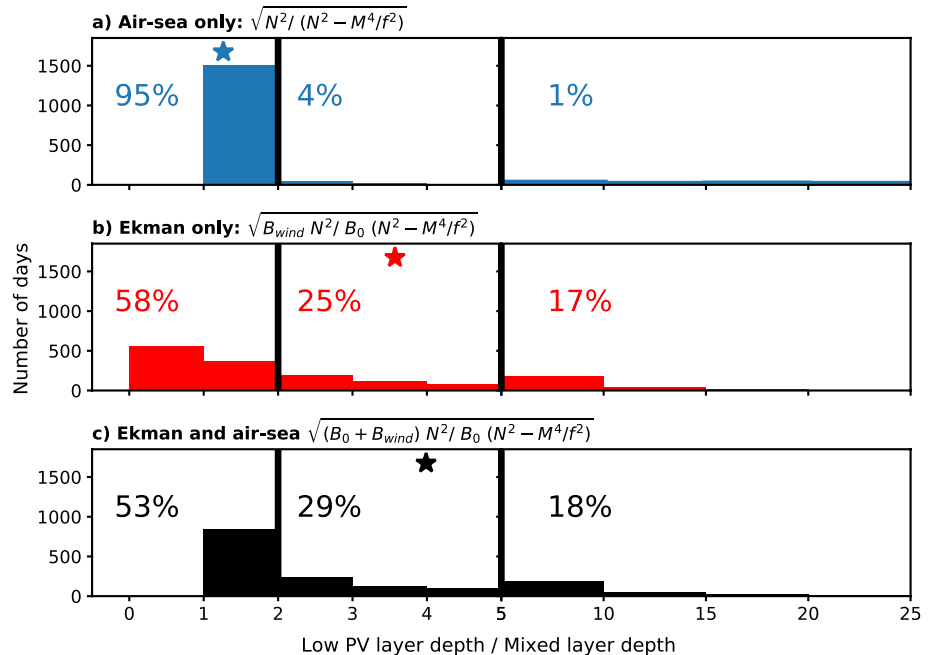


Figure 5. Histogram of the ratio of the depth of the low-PV layer formed via slantwise convection to the conventionally derived mixed layer depth. The distribution of the ratio within the boundary current (CF5) is shown, based on observed air–sea and wind forcing and vertical and horizontal density gradients. The fraction of days for which the ratio is less than 2, between 2 and 5, and greater than 5 is noted. Stars indicate the mean ratio for each forcing configuration. The horizontal axis and bin size changes at a ratio of 5.

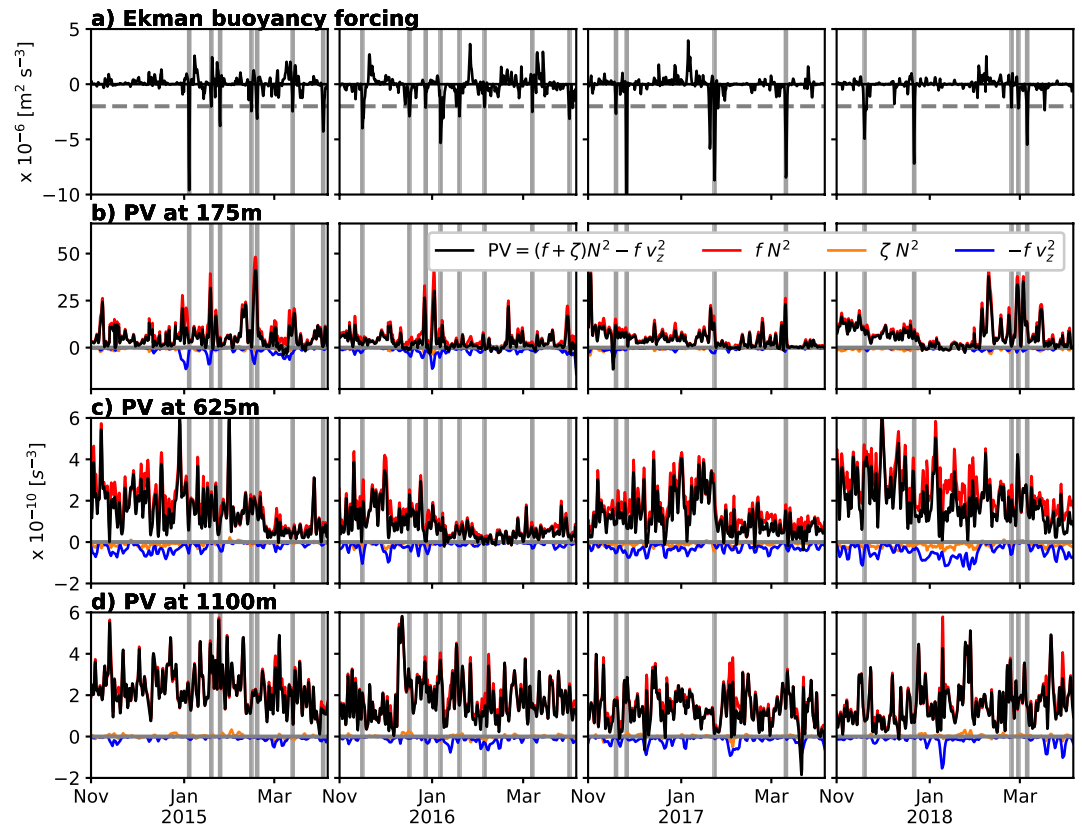


Figure 6. Atmospheric forcing and deep ocean response at the boundary current maximum, CF5, from November to April 2014–2018. (a) Ekman buoyancy forcing; gray shaded areas in all panels indicate times at which the magnitude of the negative Ekman buoyancy forcing exceeds $7.5 \times 10^{-7} \text{ m}^2 \text{ s}^{-3}$ (horizontal dotted line). (b, c, d) Potential vorticity (PV) and its components at 175, 625, and 1,100 m respectively. Strong down-front wind forcing events are associated with drops in PV throughout the water column.

We identify 26 individual events in our four-year record. On average, the Ekman buoyancy forcing is elevated for 2 days (Figure 8a). During this time, the PV decreases throughout the water column at CF5 (Figures 8b and 8c). The fact that we observe a relatively uniform subsurface PV response in our mooring data is remarkable given that events are identified based primarily on reanalysis wind stress data. One exception is the PV at 625 m, which is located in the PV minimum associated with intermediate water. The PV is particularly noisy and uncertain at this depth as there is a wide range of stratifications at this depth (Figure 6c).

The composite event also reveals the evolution of the full boundary current structure in response to down-front winds (Figures 8d–8g). At the beginning of the composite event, low salinity waters extend into the core of the boundary current, corresponding to significant horizontal and vertical buoyancy gradients. This is reflected in the high PV over the shelfbreak. Just after the event, the low salinity waters have been pushed onshore and isopycnals have steepened. PV has decreased throughout the shelfbreak area, particularly onshore of CF6, where the Ekman buoyancy forcing is strongest (Figures 3 and 4). Note that PV decreases below the conventionally defined mixed layer over the course of the composite event (green line in Figures 8f and 8g), consistent with our expectations for slantwise convection.

There is some indication that the PV drops are preceded by an increase in PV (Figures 8a–8c), which may be associated with an offshore excursion of the front that would act to increase the magnitude of the Ekman buoyancy forcing. We stress that slantwise convection would result in irreversible mixing regardless of whether there are concurrent frontal excursions. There are also many decreases in PV that are not associated with strong Ekman buoyancy (Figure 6); these may be linked to upstream forcing or frontal excursions. Note that the largest surface heat loss events are less than a tenth the size of the strong Ekman buoyancy forcing events, so the deep PV drops at CF5 are unlikely to be linked to local surface heat loss (Figure 3).

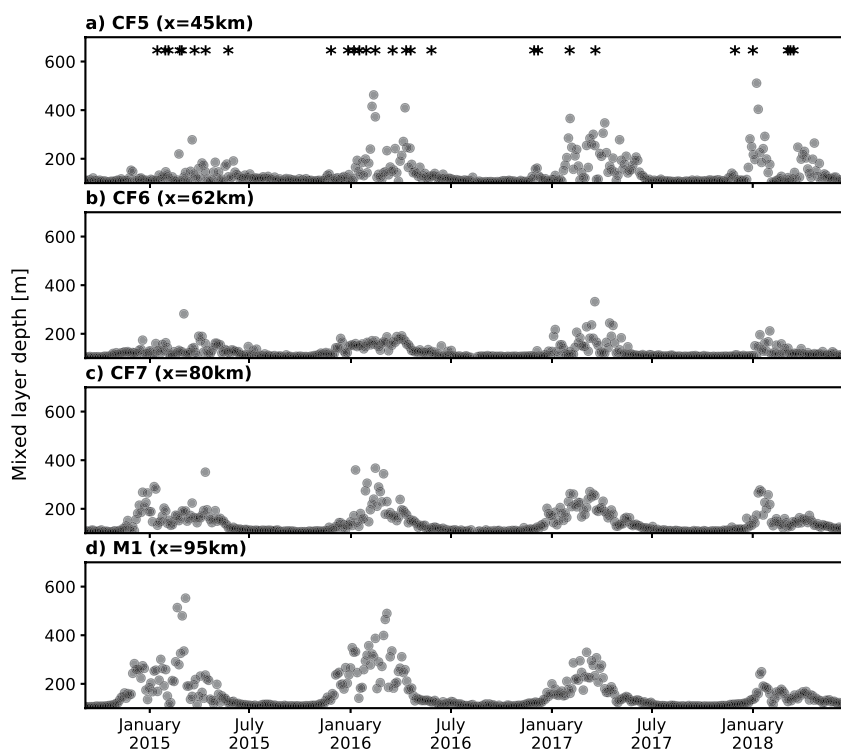


Figure 7. Three-day average vertical mixed layer depth calculated from mooring observations. Stars in panel a indicate down-front wind forcing events.

Zonal absolute momentum is another useful quantity to consider with regards to slantwise convection. When zonal absolute momentum contours are tilted relative to vertical, this indicates that slantwise effects are likely to be significant. After slantwise convection, we expect density surfaces and zonal absolute momentum surfaces to be aligned (Haine & Marshall, 1998; Straneo, Kawase, & Riser, 2002). In our composite event, we find that the zonal absolute momentum surfaces and density contours at CF5 are tilted relative to each other before the event, but are more closely aligned afterward (Figure 8). This is broadly consistent with slantwise convection at this site.

3.4. Water Mass Transformations and Property Changes

Le Bras et al. (2020) identified a water mass associated with low PV in the Irminger Sea's western boundary current and called it upper ISIW to distinguish it from the deep ISIW formed in the interior of the basin. They define the upper ISIW density range based on low stratification and a subsurface salinity maximum in winter; upper ISIW is associated with the transformation of Atlantic Waters of subtropical origin (Le Bras et al., 2020). We now suggest that slantwise convection plays a role in upper ISIW formation.

Upper ISIW formation is characterized by both salinity and temperature changes. Atlantic Waters become denser each year through cooling, and freshen as they mix with surrounding fresher waters. Hence, the salinity maximum associated with Atlantic Waters becomes fresher and sinks as it cools each winter (Figure 9b). As the buoyancy gradient between Arctic and subtropical waters is associated with a salinity front, down-front winds act to mix salinity onshore and downward, that is, the negative Ekman buoyancy forcing we observe is analogous to brine rejection rather than cooling. At the same time, as the Atlantic Waters are mixed below the very fresh light waters near the surface, they encounter waters that are of an intermediate saltiness and denser than Atlantic Waters because they are colder. So, slantwise convection likely plays a multifaceted role in this seasonal erosion of the Atlantic Water salinity maximum and the mixing of waters at this complex front.

The boundary current freshens significantly toward the end of our 4 year record (Figure 9b) (Biló et al., 2022). This results in an overall freshening of the subtropical Atlantic salinity maximum. Though the previously defined upper ISIW density range does not thicken seasonally from 2016 to 2018 as much as it did from 2014 to 2016

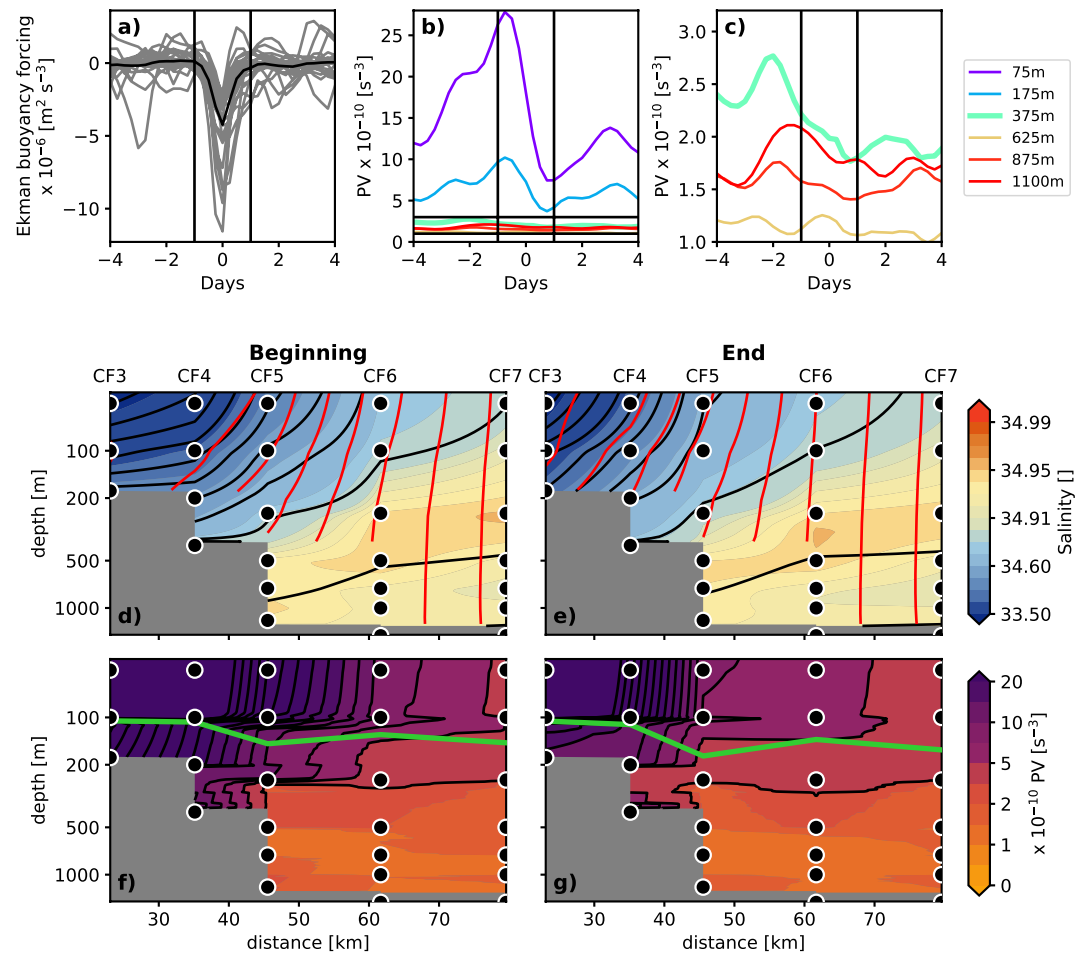


Figure 8. Evolution of a composite down-front wind event. (a) Ekman buoyancy forcing during all slantwise convection events. The gray lines are all events, and the black line is the composite mean. (b) Composite mean potential vorticity (PV) at the CF5 mooring between each of its instruments. The black horizontal lines indicate the range shown in panel (c). The black vertical lines in panels (a–c) indicate the beginning and end of the composite event, which are the focus of panels (d–g). (d, e) Salinity, shown with σ_θ isopycnals separated by 0.1 kg m^{-3} in black and zonal absolute momentum contours separated by 1 m s^{-1} in red. (f, g) PV shown with black contours separated by $2.5 \times 10^{-10} \text{ s}^{-3}$, with an upper bound mixed layer depth estimate shown in green. Note that the vertical scale is logarithmic in panels (d–g). Black circles indicate nominal moored instrument locations.

(black contours in Figure 9), lighter waters in the boundary current are modified (shoaling gray contour in Figure 9). In other words, the water mass transformations and mixing processes continue in the boundary current, but they occur in lighter, fresher waters than in past years. We suggest that the upper ISIW density range requires re-evaluation as properties change interannually, as is done for Labrador Sea Water (Yashayaev & Loder, 2016a).

Despite the long-term freshening, we continue to observe subsurface PV responses to down-front wind events (Figures 6 and 9a). In contrast, the mixed layers offshore shoal as the water column freshens (Figure 7). In general, mixed layers are deeper and more persistent offshore. At CF5, the boundary current maximum, deep mixed layers are sporadic and there is deepening associated with down-front wind forcing events that is not seen at CF6. This is likely because upright and slantwise convection are coupled, resulting in some vertical homogenization of density. It is also possible that we overestimate the depth of the mixed layer as our observations are subsurface, and that this calculation is influenced by subsurface homogeneous layers.

In sum, we suggest that slantwise convection plays a role in the seasonal transformation of Atlantic Waters and find that this process persists despite the long-term freshening of Atlantic Waters. This implies that slantwise convection may be more resilient to freshening than vertical convection is, as long as horizontal density gradients (and winds) persist.

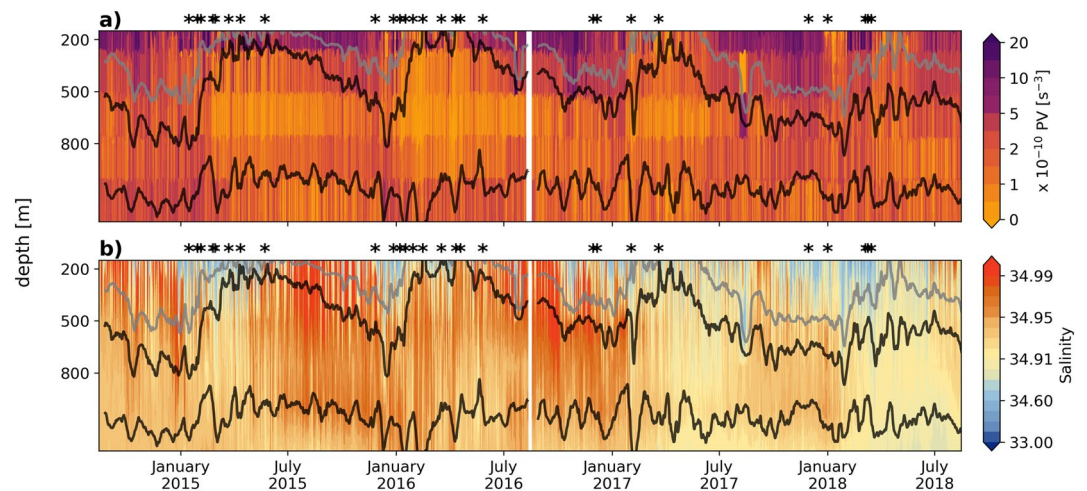


Figure 9. Temporal evolution of daily (a) Potential Vorticity (PV) and (b) salinity at the boundary current maximum (CF5). Black isopycnals mark the boundaries of upper ISIW, $\sigma_\theta = 27.65\text{--}27.73 \text{ kg m}^{-3}$; the gray contour is the $\sigma_\theta = 27.6 \text{ kg m}^{-3}$ isopycnal. Stars at the top of each panel indicate down-front wind forcing events.

4. Discussion

4.1. Uncertainty

There is significant uncertainty in our PV estimate due to the limitations of our observations. We are only able to calculate the across-section component of relative vorticity, and we apply the thermal wind balance as we resolve vertical gradients better than horizontal gradients near the continental slope. The most significant source of uncertainty is the horizontal spacing between the moorings, which limits the horizontal gradients we can resolve and can lead to aliasing. We estimate that the error in the PV may be up to several times its calculated value. Our interpretations are hence based primarily on the temporal evolution of PV rather than its absolute value.

The subsurface ocean response is consistent with our expectation that the low-PV layer is deeper than the mixed layer during down-front wind forcing events. However, a direct quantification of the low-PV layer from our observations is complicated by the fact that we do not fully resolve PV. Furthermore, as our observations do not extend to the surface, the mixed layer depths we estimate are potentially an overestimate; the fact that PV is affected below this upper bound emphasizes that the water column is responding well below the mixed layer.

We would expect to observe areas of negative or zero PV, which are tell-tale signs of symmetric instability. While the observations are consistent with the presence of these areas, the moorings do not resolve PV well enough to show this explicitly. The relative vorticity term (ζN^2) and the shear term ($-f v_z^2$) both counter the dominant vertical buoyancy gradient term ($f N^2$) within the boundary current (Figure 6) and measuring these more accurately would likely decrease the PV further.

4.2. Large-Scale Context

Slantwise convection is forced by extreme wind events, which in this region are usually associated with cyclones that interact with Greenland's high topography (Doyle & Shapiro, 1999; Josey et al., 2019; Moore & Renfrew, 2005). A cyclone approaching from the west would cause southerly winds followed by northerly winds, consistent with our observation that, during some events, boundary current waters are first pushed offshore before being pushed back onshore (Figure 8). To investigate whether the down-front wind forcing events at the moorings were associated with a particular atmospheric pattern, we made a composite of sea level pressure anomaly. We found that the peak Ekman buoyancy forcing of our composite slantwise convection event is associated with a cyclone southeast of Greenland (Figure 10), suggesting that slantwise convection in this region is largely driven by synoptic-scale atmospheric features. However, the progression of the atmospheric low varied substantially from event to event and did not point to one type of atmospheric event that consistently led to strong down-front winds at the mooring location.

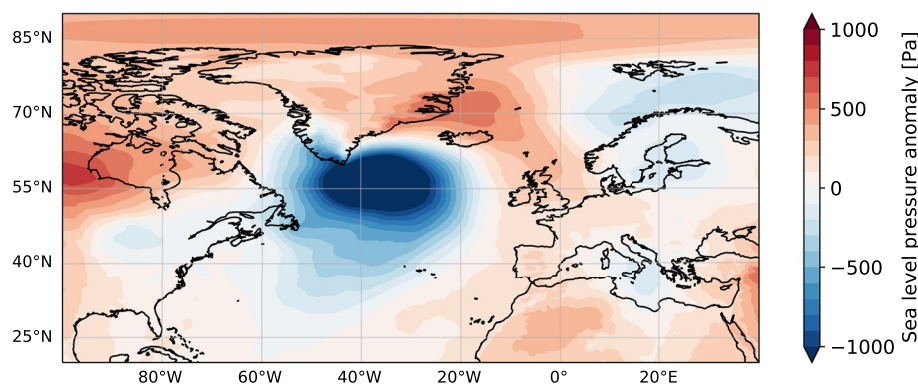


Figure 10. Composite of sea level pressure anomaly centered at the maximum Ekman buoyancy forcing at CF5. Anomalies are taken from the July 2014–July 2018 time mean at each point.

Our observations, together with the large-scale wind stress, density, and ocean circulation patterns, suggest that slantwise convection could occur all along the east coast of Greenland and in the western Labrador Sea (Figure 1a). Hence, waters transformed by slantwise convection in the Irminger Sea may be re-ventilated by slantwise convection in the Labrador Sea. A similar process likely also occurs in the western Nordic Seas (Våge et al., 2018). We estimate the relative importance of slantwise and upright convection in the Irminger Sea using our finding that the Ekman buoyancy forcing is four times the air–sea buoyancy forcing over the boundary current (Figure 1d). To do this, we define western boundary and interior regions of the Irminger Sea and compare the total heat flux over both regions with the deduced Ekman buoyancy flux over the western boundary region (Figure 1a). This back-of-the-envelope calculation suggests that Ekman buoyancy fluxes are on the order of the air–sea heat fluxes integrated over the entire Irminger Sea, which is notable given that the basin interior covers a much larger area than the western boundary region. Slantwise convection may also occur in the interior of subpolar basins (symmetric instabilities have been observed in open ocean environments with transient fronts), but we currently lack the observations necessary to quantify this.

The water column freshened over the course of our 4-year record, causing the mixed layer depth to decrease offshore of the boundary current (Figures 7 and 9). Slantwise convection, however, was more resilient than upright convection to this change; we observe a deep PV response to down-front winds despite the changing water mass properties (Figures 6 and 9). We hypothesize that this is because the horizontal density gradient between salty Atlantic-origin and fresh Arctic-origin waters persisted despite the freshening of the Atlantic-origin waters. As freshwater sources to the subpolar North Atlantic increase, we may find an increasing role for slantwise convection relative to upright convection. However, we note that there is likely important interplay between upright and slantwise convection. The stratification is low in this region due to upright convection, which is important pre-conditioning that makes the water column generally susceptible to slantwise convection. Furthermore, during a down-front wind event, the initial response to the Ekman buoyancy forcing may be upright convection, which then triggers symmetric instability and finally adjustment via slantwise convection.

4.3. Outlook for Modeling and Observations

Although it is possible to parameterize slantwise convection in numerical models, successful implementation requires that sharp horizontal density gradients are resolved (Bachman et al., 2017; Thomas, 2005; Thomas & Lee, 2005). Gula et al. (2014) found that even with 500 m horizontal resolution, they did not fully resolve symmetric instability in the Gulf Stream region, and Dong et al. (2021) estimated that ≈ 100 m horizontal scales need to be resolved to simulate symmetric instability in the subpolar boundary regions. The salinity fronts of the subpolar North Atlantic present a particular challenge as most ocean models are prone to salinity drifts and do not reliably simulate fresh water fluxes from Greenland and the Arctic (Böning et al., 2016; Danabasoglu et al., 2016; Dukhovskoy et al., 2016).

Field campaigns elsewhere have resolved the horizontal structure of PV during down-front wind events using towed instruments and gliders (Adams et al., 2017; Bosse et al., 2021; Carpenter et al., 2020; Joyce et al., 2009; Peng et al., 2020; Thomas et al., 2013, 2016; Thompson et al., 2016; Yu et al., 2019). Given the harsh conditions

in the Irminger Sea, a winter glider survey is the most promising avenue for better resolving this process in the future. Previous studies have observed the subduction of high oxygen and high chlorophyll waters associated with down-front wind–forced instabilities (Bosse et al., 2021; Joyce et al., 2009; Thomas et al., 2013). This implies that slantwise convection may be an important contributor to the ventilation of the deep Atlantic. Oxygen sensors were deployed on the Irminger and Labrador Sea OSNAP moorings in the summer of 2020. The resulting data will provide valuable information on the coupling of water mass transformation via slantwise convection with ventilation and biogeochemical cycling.

5. Conclusions

We have presented observational evidence consistent with slantwise convection in the Irminger Sea's western boundary current. Strong winds blowing in the same direction as the current push denser waters onshore over lighter waters (Figure 2). Over our 4-year record, we identified 26 down-front wind forcing events, which coincide with a subsurface decrease in PV below the conventionally defined surface mixed layer (Figure 8). We estimate that the Ekman buoyancy forcing is four times as strong as the air–sea buoyancy forcing over the boundary current (Figure 4), and that slantwise convection impacts the water column to four times the conventionally defined mixed layer depth on average (Figure 5).

Interestingly, the down-front winds push saltier water over fresher water, and are hence analogous to evaporation or brine rejection rather than cooling. Since slantwise convection necessarily brings fresh continental shelf waters into contact with saltier denser waters of a different origin, proper representation of salinity fronts and slantwise convection in ocean models will likely improve their representation of subpolar water mass transformations, as well as associated carbon and heat fluxes.

Data Availability Statement

OSNAP mooring data used in this study are available at <http://www.o-snap.org/observations/data/> under “US East Cape Farewell Slope Array.” ERA5 reanalysis hourly data was downloaded from <https://cds.climate.copernicus.eu/cdsapp%23%21/dataset/reanalysis%2Dera5%2Dsingle%2Dlevels>. Hourly wind stress and heat flux fields were downloaded on June 18, 2020 and hourly sea level pressure data was downloaded on July 13, 2021. ERA5 monthly wind stress fields shown in Figure 1 were downloaded on August 4, 2020 from <https://cds.climate.copernicus.eu/cdsapp%23%21/dataset/reanalysis%2Dera5%2Dsingle%2Dlevels%2Dmonthly%2Dmeans>. Monthly sea surface height (anomaly) data (Figure 1) are Ssalto/Duacs altimeter products distributed by Aviso+ with support from Cnes and by the Copernicus Marine and Environment Monitoring Service (CMEMS). They were downloaded on August 31, 2020 from https://resources.marine.copernicus.eu/product-detail/SEALEVEL_GLO_PHY_L4_MY_008_047.

Acknowledgments

I. A.-A. Le Bras, F. Straneo, T. C. Biló, and J. Holte gratefully acknowledge the US National Science Foundation (NSF): this work was supported by grants OCE-1258823, OCE-1756272, OCE-1948335, and OCE-2038481. J. Callies gratefully acknowledges NSF support through grant OCE-1924354. H. L. Johnson was supported by the SNAP-DRAGON program (UK Natural Environment Research Council grant number NE/T013494/1). The authors gratefully acknowledge the many scientists and mariners who went to sea to collect the observational data, and Bob Pickart in particular.

References

- Adams, K. A., Hosegood, P., Taylor, J. R., Sallée, J. B., Bachman, S., Torres, R., & Stamper, M. (2017). Frontal circulation and submesoscale variability during the formation of a southern ocean mesoscale eddy. *Journal of Physical Oceanography*, 47, 1737–1753. <https://doi.org/10.1175/JPO-D-16-0266.1>
- Bachman, S. D., Fox-Kemper, B., Taylor, J. R., & Thomas, L. N. (2017). Parameterization of frontal symmetric instabilities. I: Theory for resolved fronts. *Ocean Modelling*, 109, 72–95. <https://doi.org/10.1016/j.ocemod.2016.12.003>
- Biló, T. C., Straneo, F., Holte, J., & Le Bras, I. A. (2022). Arrival of new great salinity anomaly weakens convection in the Irminger Sea. *Geophysical Research Letters*, 49, e2022GL098857. <https://doi.org/10.1029/2022gl098857>
- Böning, C. W., Behrens, E., Biastoch, A., Getzlaff, K., & Bamber, J. L. (2016). Emerging impact of Greenland meltwater on deepwater formation in the North Atlantic Ocean. *Nature Geoscience*, 9, 523–527. <https://doi.org/10.1038/ngeo2740>
- Bosse, A., Testor, P., Damien, P., Estournel, C., Marsaleix, P., Mortier, L., et al. (2021). Wind-forced submesoscale symmetric instability around deep convection in the northwestern mediterranean sea. *Fluids*, 6, 1–27. <https://doi.org/10.3390/fluids603012>
- Brambilla, E., & Talley, L. D. (2008). Subpolar mode water in the northeastern Atlantic: 1. Averaged properties and mean circulation. *Journal of Geophysical Research*, 113, C04025. <https://doi.org/10.1029/2006JC004062>
- Brambilla, E., Talley, L. D., & Robbins, P. E. (2008). Subpolar mode water in the northeastern Atlantic: 2. Origin and transformation. *Journal of Geophysical Research*, 113, C04026. <https://doi.org/10.1029/2006JC004063>
- Buckingham, C. E., Lucas, N. S., Belcher, S. E., Rippeth, T. P., Grant, A. L., Le Sommer, J., et al. (2019). The contribution of surface and submesoscale processes to turbulence in the open ocean surface boundary layer. *Journal of Advances in Modeling Earth Systems*, 11, 4066–4094. <https://doi.org/10.1029/2019MS001801>
- Carpenter, J. R., Rodrigues, A., Schultze, L. K., Merckelbach, L. M., Suzuki, N., Baschek, B., & Umlauf, L. (2020). Shear instability and turbulence within a submesoscale front following a storm. *Geophysical Research Letters*, 47, e2020GL090365. <https://doi.org/10.1029/2020GL090365>

- D'Asaro, E., Lee, C., Rainville, L., Harcourt, R., & Thomas, L. (2011). Enhanced turbulence and energy dissipation at ocean fronts. *Science*, 332, 318–322. <https://doi.org/10.1126/science.1201515>
- Danabasoglu, G., Yeager, S. G., Kim, W. M., Behrens, E., Bentsen, M., Bi, D., et al. (2016). North Atlantic simulations in coordinated ocean-ice reference experiments phase II (CORE-II). Part II: Inter-annual to decadal variability. *Ocean Modelling*, 97, 65–90. <https://doi.org/10.1016/j.ocemod.2015.11.007>
- Daniault, N., Lherminier, P., & Mercier, H. (2011). Circulation and transport at the southeast tip of Greenland. *Journal of Physical Oceanography*, 41, 437–457. <https://doi.org/10.1175/2010JPO4428.1>
- Dee, D. P., Uppala, S. M., Simmons, A. J., Berrisford, P., Poli, P., Kobayashi, S., et al. (2011). The ERA-interim reanalysis: Configuration and performance of the data assimilation system. *Quarterly Journal of the Royal Meteorological Society*, 137, 553–597. <https://doi.org/10.1002/qj.828>
- De Jong, M. F., Oltmanns, M., Karstensen, J., & De Steur, L. (2018). Deep convection in the Irminger Sea observed with a dense mooring array. *Oceanography*, 31(1), 50–59. <https://doi.org/10.5670/oceanog.2018.109>
- Dickson, R. R., & Brown, J. (1994). The production of North Atlantic deep water: Sources, rates, and pathways. *Journal of Geophysical Research*, 99, 12319–12341. <https://doi.org/10.1029/94JC00530>
- Dong, J., Fox-Kemper, B., Zhang, H., & Dong, C. (2021). The scale and Activity of symmetric instability estimated from a global submesoscale-permitting ocean model. *Journal of Physical Oceanography*, 51, 1655–1670. <https://doi.org/10.1175/JPO-D-20-0159.1>
- Doyle, J. D., & Shapiro, M. A. (1999). Flow response to large-scale topography: The Greenland tip jet. *Tellus*, 51, 728–748. <https://doi.org/10.1034/j.1600-0870.1996.00014.x>
- Dukhovskoy, D. S., Myers, P. G., Platov, G., Timmermans, M., Curry, B., Proshutinsky, A., et al. (2016). Greenland freshwater pathways in the sub-Arctic Seas from model experiments with passive tracers. *Journal of Geophysical Research: Oceans*, 121, 877–907. [https://doi.org/10.1002/2015JC011290@10.1002/\(ISSN\)2169-9291.FAMOS1](https://doi.org/10.1002/2015JC011290@10.1002/(ISSN)2169-9291.FAMOS1)
- Giordani, H., Lebeaupin-Brossier, C., Léger, F., & Caniaux, G. (2017). A PV-approach for dense water formation along fronts: Application to the Northwestern Mediterranean. *Journal of Geophysical Research: Oceans*, 122, 995–1015. <https://doi.org/10.1002/2016JC012019>
- Gula, J., Molemaker, J. J., & McWilliams, J. C. (2014). Submesoscale cold filaments in the gulf stream. *Journal of Physical Oceanography*, 44, 2617–2643. <https://doi.org/10.1175/JPO-D-14-0029.1>
- Haine, T. W., & Marshall, J. (1998). Gravitational, symmetric, and baroclinic instability of the ocean mixed layer. *Journal of Physical Oceanography*, 28, 634–658. [https://doi.org/10.1175/1520-0485\(1998\)028<0634:GSABIO>2.0.CO;2](https://doi.org/10.1175/1520-0485(1998)028<0634:GSABIO>2.0.CO;2)
- Harden, B. E., & Renfrew, I. A. (2012). On the spatial distribution of high winds off southeast Greenland. *Geophysical Research Letters*, 39. <https://doi.org/10.1029/2012GL052245>
- Hoskins, B. J. (1974). The role of potential vorticity in symmetric stability and instability. *Quarterly Journal of the Royal Meteorological Society*, 100, 480–482. <https://doi.org/10.1093/cdj/3.1.2>
- Huang, J., Pickart, R. S., Huang, R. X., Lin, P., Brakstad, A., & Xu, F. (2020). Sources and upstream pathways of the densest overflow water in the Nordic Seas. *Nature Communications*, 11, 1–9. <https://doi.org/10.1038/s41467-020-19050-y>
- Josey, S. A., De Jong, M. F., Oltmanns, M., Moore, G. K., & Weller, R. A. (2019). Extreme variability in Irminger Sea winter heat loss revealed by ocean observatories initiative mooring and the ERA5 reanalysis. *Geophysical Research Letters*, 46, 293–302. <https://doi.org/10.1029/2018GL080956>
- Joyce, T. M., Thomas, L. N., & Bahr, F. (2009). Wintertime observations of subtropical mode water formation within the gulf stream. *Geophysical Research Letters*, 36, L02607. <https://doi.org/10.1029/2008GL035918>
- Joyce, T. M., Thomas, L. N., Dewar, W. K., & Garton, J. B. (2013). Eighteen degree water formation within the gulf stream during CLIMODE. *Deep-Sea Research Part II Topical Studies in Oceanography*, 91, 1–10. <https://doi.org/10.1016/j.dsr2.2013.02.019>
- Le Bras, I., Straneo, F., Holte, J., De Jong, M. F., & Holliday, N. P. (2020). Rapid export of waters formed by convection near the Irminger Sea's western boundary. *Geophysical Research Letters*, 47. <https://doi.org/10.1029/2019GL085989>
- Le Bras, I., Straneo, F., Holte, J., & Holliday, N. P. (2018). Seasonality of freshwater in the east Greenland current system from 2014 to 2016. *Journal of Geophysical Research: Oceans*, 123. <https://doi.org/10.1029/2018JC014511>
- Moore, G. W. K., Pickart, R. S., & Renfrew, I. A. (2008). Buoy observations from the windiest location in the world ocean, Cape Farewell, Greenland. *Geophysical Research Letters*, 35, 3–7. <https://doi.org/10.1029/2008GL034845>
- Moore, G. W. K., & Renfrew, I. A. (2005). Tip jets and barriers winds: A QuickSCAT climatology of high wind speed events around Greenland. *Journal of Climate*, 18, 4919. <https://doi.org/10.1175/JCLI9007.1>
- Peng, J. P., Holtermann, P., & Umlauf, L. (2020). Frontal instability and energy dissipation in a submesoscale upwelling filament. *Journal of Physical Oceanography*, 50, 2017–2035. <https://doi.org/10.1175/JPO-D-19-0270.1>
- Petit, T., Lozier, M. S., Josey, S. A., & Cunningham, S. A. (2020). Atlantic deep water formation occurs primarily in the Iceland basin and Irminger Sea by local buoyancy forcing. *Geophysical Research Letters*, 47, 1–9. <https://doi.org/10.1029/2020GL091028>
- Pickart, R. S., Smethie, W. M., Lazier, J. R. N., Jones, E. P., & Jenkins, W. J. (1996). Eddies of newly formed upper Labrador Sea water. *Journal of Geophysical Research*, 101, 20711–20726. <https://doi.org/10.1029/96JC01453>
- Straneo, F., Kawase, M., & Pickart, R. S. (2002). Effects of wind on convection in strongly and weakly baroclinic flows with application to the Labrador Sea. *Journal of Physical Oceanography*, 32, 2603–2618. [https://doi.org/10.1175/1520-0485\(2002\)32<2603:JPO>2.0.CO;2](https://doi.org/10.1175/1520-0485(2002)32<2603:JPO>2.0.CO;2)
- Straneo, F., Kawase, M., & Riser, S. C. (2002). Idealized models of slantwise convection in a baroclinic flow. *Journal of Physical Oceanography*, 32, 558–572. [https://doi.org/10.1175/1520-0485\(2002\)032<0558:IMOSCI>2.0.CO;2](https://doi.org/10.1175/1520-0485(2002)032<0558:IMOSCI>2.0.CO;2)
- Swift, J. H. (1984). The circulation of the Denmark Strait and Iceland-Scotland overflow waters in the North Atlantic. *Deep Sea Research*, 31, 1339–1355. [https://doi.org/10.1016/0198-0149\(84\)90005-0](https://doi.org/10.1016/0198-0149(84)90005-0)
- Talley, L. D., & McCartney, M. S. (1982). Distribution and circulation of Labrador Sea water. *Journal of Physical Oceanography*, 12, 1189–1205. [https://doi.org/10.1175/1520-0485\(1982\)012<1189:DACOLS>2.0.CO;2](https://doi.org/10.1175/1520-0485(1982)012<1189:DACOLS>2.0.CO;2)
- Taylor, J. R., & Ferrari, R. (2010). Buoyancy and wind-driven convection at mixed layer density fronts. *Journal of Physical Oceanography*, 40, 1222–1242. <https://doi.org/10.1175/2010JPO4365.1>
- Thomas, L. N. (2005). Destruction of potential vorticity by winds. *Journal of Physical Oceanography*, 35, 2457–2466. <https://doi.org/10.1175/JPO2830.1>
- Thomas, L. N., & Lee, C. M. (2005). Intensification of ocean fronts by down-front winds. *Journal of Physical Oceanography*, 35, 1086–1102. <https://doi.org/10.1175/JPO2737.1>
- Thomas, L. N., & Taylor, J. R. (2010). Reduction of the useable wind-work on the general circulation by forced symmetric instability. *Geophysical Research Letters*, 37, L18606. <https://doi.org/10.1029/2010GL044680>
- Thomas, L. N., Taylor, J. R., D'Asaro, E. A., Lee, C. M., Klymak, J. M., & Shcherbina, A. (2016). Symmetric instability, inertial oscillations, and turbulence at the gulf stream front. *Journal of Physical Oceanography*, 46, 197–217. <https://doi.org/10.1175/JPO-D-15-0008.1>

- Thomas, L. N., Taylor, J. R., Ferrari, R., & Joyce, T. M. (2013). Symmetric instability in the gulf stream. *Deep-Sea Research Part II Topical Studies in Oceanography*, 91, 96–110. <https://doi.org/10.1016/j.dsr2.2013.02.025>
- Thompson, A. F., Lazar, A., Buckingham, C., Garabato, A. C., Damerell, G. M., & Heywood, K. J. (2016). Open-ocean submesoscale motions: A full seasonal cycle of mixed layer instabilities from gliders. *Journal of Physical Oceanography*, 46, 1285–1307. <https://doi.org/10.1175/JPO-D-15-0170.1>
- Våge, K., Papritz, L., Håvik, L., Spall, M. A., & Moore, G. W. (2018). Ocean convection linked to the recent ice edge retreat along east Greenland. *Nature Communications*, 9, 1287. <https://doi.org/10.1038/s41467-018-03468-6>
- Viglione, G. A., Thompson, A. F., Flexas, M. M., Sprintall, J., Swart, S., Viglione, G. A., et al. (2018). Abrupt transitions in submesoscale structure in southern drake passage: Glider observations and model results. *Journal of Physical Oceanography*, 48, 2011–2027. <https://doi.org/10.1175/JPO-D-17-0192.1>
- Yashayev, I., & Loder, J. W. (2016a). Further intensification of deep convection in the Labrador Sea in 2016. *Geophysical Research Letters*, 44, 1429–1438. <https://doi.org/10.1002/2013GL058740>.Received
- Yashayev, I., & Loder, J. W. (2016b). Recurrent replenishment of Labrador Sea water and associated decadal-scale variability. *Journal of Geophysical Research: Oceans*, 121, 8095–8114. <https://doi.org/10.1002/2016JC012046>
- Yu, X., Naveira Garabato, A. C., Martin, A. P., Evans, D. G., & Su, Z. (2019). Wind-forced symmetric instability at a transient mid-ocean front. *Geophysical Research Letters*, 46, 11281–11291. <https://doi.org/10.1029/2019GL084309>